

JGR Solid Earth

RESEARCH ARTICLE

10.1029/2019JB017792

Key Points:

- A slurry layer and a compacting cumulate pile form at the base of the outer core and the top of the inner core, respectively
- The slurry layer with light element partitioning can explain the observed reduced velocity gradient at the base of the outer core
- The compacting cumulate pile may exhibit lateral variations across the inner-core boundary, causing the east-west seismic wave velocity asymmetry

Supporting Information:

- Supporting Information S1

Correspondence to:

Y. Zhang and J.-F. Lin,
afu@jsg.utexas.edu;
zhangyoujun@scu.edu.cn

Citation:

Zhang, Y., Nelson, P., Dygert, N., & Lin, J.-F. (2019). Fe alloy slurry and a compacting cumulate pile across Earth's inner-core boundary. *Journal of Geophysical Research: Solid Earth*, 124, 10,954–10,967. <https://doi.org/10.1029/2019JB017792>

Received 4 APR 2019

Accepted 1 OCT 2019

Accepted article online 22 OCT 2019

Published online 8 NOV 2019

Fe Alloy Slurry and a Compacting Cumulate Pile Across Earth's Inner-Core Boundary

Youjun Zhang¹ , Peter Nelson², Nick Dygert^{2,3} , and Jung-Fu Lin² 

¹Institute of Atomic and Molecular Physics, Sichuan University, Chengdu, China, ²Department of Geological Sciences, Jackson School of Geosciences, University of Texas at Austin, Austin, TX, USA, ³Planetary Geoscience Institute, Department of Earth and Planetary Sciences, University of Tennessee, Knoxville, TN, USA

Abstract Seismic observations show a reduced compressional-wave velocity gradient at the base of the outer core relative to the preliminary reference Earth model and seismic wave asymmetry between the east-west hemispheres at the top of the inner core. Here we propose a model for the inner core boundary (ICB), where a slurry layer forms through fractional crystallization of an Fe alloy at the base of the outer core (F layer) above a compacting cumulate pile at the top of the inner core (F' layer). Using recent mineral physics data, we show that fractional crystallization of an Fe alloy (e.g., Fe-Si-O) with a solid fraction of $\sim 15 \pm 5\%$ and preferential light element partitioning into the liquid can explain the observed reduced velocity gradient in the F layer. The compacting cumulate pile in the F' layer may exhibit lateral variations in thickness between the east-west hemispheres due to lateral variations of large-scale heat flux in the outer core, which may explain the east-west asymmetry observed in the seismic velocity. Our model suggests that the inner core solid has a high shear viscosity $>10^{22}$ Pa/s.

Plain Language Summary Seismic observations show a reduced P wave velocity gradient layer at the bottom ~ 280 km of the outer core and a hemispherical dichotomy at the top ~ 50 – 200 km of the inner core compared to the one-dimensional Preliminary reference Earth model (PREM). These seismic features manifest physical and chemical phenomena linked to thermal evolution and formation processes of the inner core. We have developed a physical model to explain these seismic features. At the inner-outer boundary, the crystallization of Fe alloy co-exists with the residue melt producing a “snowing” slurry layer (F layer), consistent with observed seismic velocity gradient. Solid Fe alloy crystals accumulate and eventually compact at the top of the inner core, and may exhibit lateral variations in thickness between the east-west hemispheres. Our model can explain the east-west asymmetry observed in the seismic velocity. Our model uses mineral physics and seismological results to provide a holistic view of the physical and chemical processes for the inner-core growth over geological time.

1. Introduction

Our knowledge of the Earth's core is mainly derived from seismic observations and mineral physics studies, which suggest that the core comprises of a solid inner core surrounded by a liquid outer core with Fe-Ni and some light element(s) alloy (Hirose et al., 2013; Li & Fei, 2014). The inner core grows as the molten outer core cools and solidifies, releasing latent heat and gravitational energy that drives the geodynamo and generates Earth's magnetic field (Buffett, 2000; Davies et al., 2015). Recently, detailed seismic studies using differential travel times and amplitudes in PKP, PKIKP, and PKiKP waves show a reduced P wave velocity (V_p) gradient layer compared to the preliminary reference Earth model (PREM) at the bottom ~ 280 km of the outer core, known as the F layer (Figure 1; Adam et al., 2018; Dziewonski & Anderson, 1981; Kennett et al., 1995; Ohtaki & Kaneshima, 2015; Song & Helmberger, 1995; Souriau & Poupinet, 1991; Zou et al., 2008). Most of these seismic observations indicate that the F layer is global, surrounding the entire inner core (Cormier et al., 2011; Souriau & Poupinet, 1991; Zou et al., 2008). Additionally, analyses of PKIKP and PKiKP waves across the region show a hemispherical dichotomy at the top ~ 50 – 200 km of the inner core which we call the F' layer (Figure 1; Deuss et al., 2010; Monnereau et al., 2010; Niu & Wen, 2001; Waszek & Deuss, 2011; Yu & Wen, 2006). In the F' layer as shown in Figure 1, the eastern hemisphere has a faster V_p than the western hemisphere (Monnereau et al., 2010). The upper ~ 50 – 100 km of the F' layer has an isotropic velocity variation of $\sim 1.5\%$ between the two hemispheres, while in the deeper part the difference decreases ($\sim 0.5\%$; Deuss, 2014). Understanding the cause of the reduced V_p gradient in the F layer and

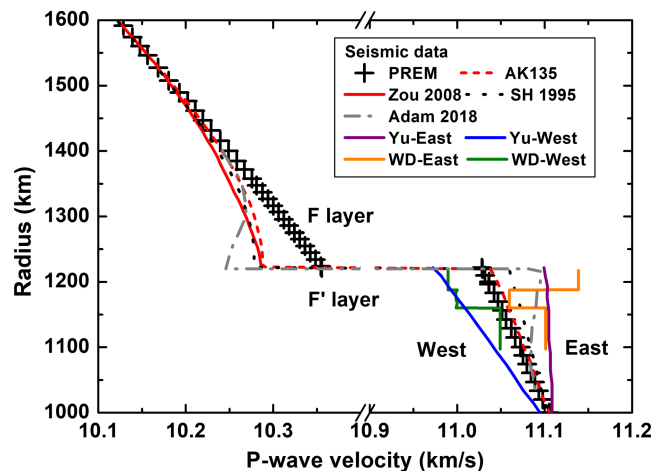


Figure 1. P wave velocity across the inner-core boundary. A velocity gradient exists in the F layer, whereas the hemispherical wave velocity asymmetry in the F' layer can be seen from the difference in velocity profiles labeled as “East” and “West”. Data from seismological observations are shown for the PREM (plus symbol line; Dziewonski & Anderson, 1981), AK135 (red-dashed line; Kennett et al., 1995), Zou 2008 (red-solid line; Zou et al., 2008), SH 1995 (black-dotted line; Song & Helmberger, 1995), Adam 2018 (gray dash-dotted line; Adam et al., 2018), Yu-East (purple line; Yu & Wen, 2006), Yu-West (blue line; Yu & Wen, 2006), WD-East (orange line; Waszek & Deuss, 2011), and WD-West (olive line; Waszek & Deuss, 2011), respectively.

hemispheric seismic velocity asymmetry in the F' layer can provide crucial constraints on the inner core's formation and related geodynamic processes. These in turn can help us understand the thermal and compositional state of the inner and outer core.

The aforementioned seismic features manifest physical and chemical properties of the constituent Fe alloy as well as solidification and thermal evolution mechanisms of the inner core (Deguen, 2012). With the recently refined seismic observations across the inner-core boundary (ICB; Figure 1; Yu & Wen, 2006; Zou et al., 2008), a number of models have been proposed to reconcile seismic observations for the F and F' layers (Deuss, 2014). Particularly, solidification or melting of Fe with light element partitioning has been suggested to cause light-element-rich or light-element-poor variations in the F layer. For example, Gubbins et al. (2008) proposed that V_p variations in the F layer can be explained by a stably stratified layer on the liquidus with compositional variations with depth due to solidification and remelting of Fe alloy (Gubbins et al., 2008). The model explains that the reduction in seismic velocity with depth is caused by light element(s) being released from the F layer. A thermochemical flow model was also proposed by Gubbins et al. (2011), arguing that variations in mantle heat flow may result in temperature variations and localized melting and freezing at the ICB due to large-scale convection patterns in the outer core. Subsequently, lateral variation at the top of the inner core such as the hemispheric asymmetry in the F' layer (Gubbins et al., 2011) may be generated. However, this model does not use mineral physics data to explain seismic observations such as the origin of the east-west hemispherical asymmetry, nor explain the processes of liquid Fe alloy crystallization (and remelting) in detail.

Another scenario for the east-west asymmetry is an inner core translation model, where the F' layer is generated by the simultaneous solidification and melting of the western and eastern hemispheres, respectively (Alboussière et al., 2010). This process results in a lateral translation of the inner core material from west to east, causing a lopsided growth of the inner core (Alboussière et al., 2010; Monnereau et al., 2010). However, this inner core translation model is unlikely because it does not explain the existence of a sharp hemispherical boundary in the F' layer (Monnereau et al., 2010). Furthermore, inner core convection may not occur if thermal conductivity is as high as recently suggested (Davies et al., 2015; Ohta et al., 2016). Thus, it remains challenging to explain the origin of the reduced seismic V_p gradient in the F layer and hemispheric asymmetry in the F' layer simultaneously.

Besides these above models, a slurry F layer was proposed in 1963 by S.I. Braginskii (1963), which explains the compositional convection process in the Earth's core. It was further investigated by a number of researchers to

understand possible formation mechanisms of the slurry layer (e.g., Fearn et al., 1981; Loper, 1983; Loper & Roberts, 1977; Loper & Roberts, 1980; Loper & Roberts, 1981; Shimizu et al., 2005; Sumita et al., 1996). A more recent study indicates that a slurry *F* layer arising from particles of iron freezing out of the liquid alloy could satisfy the geophysical constraints on the density jump across ICB and the heat flux across the core-mantle boundary (CMB; Wong et al., 2018). An approximately 100-km-thick slurry layer likely exists at the top of the present Martian core as well, according to a geodynamic model with magnetic and geodetic constraints (Davies & Pommier, 2018). Therefore, a unique core formation process may exist for terrestrial planets, where solid cores grow from the sedimentation of suspended particles snowing down from a slurry zone above their solid core boundary (Breuer et al., 2015; Buffett et al., 2000; Stewart et al., 2007; Sumita et al., 1996). A compacting pile or mushy zone may form near the top of the solid boundary as a result of the particle sedimentation in the slurry (Tian & Wen, 2017), which is partially molten, analogous to a cumulate pile at the bottom of a magma chamber (Deguen et al., 2007; McKenzie, 2011; Shirley, 1986; Sumita et al., 1996). An updated model using recent mineral physics results on density, velocities, and melting temperatures of candidate Fe alloys at relevant pressure-temperature (*P-T*) conditions of the ICB is needed to address the mechanism of the slurry formation and the consequent light element partitioning and inner core compaction.

Relevant geodynamic models proposed in the past are summarized in Table S1, and in general, they only satisfy some aspects of the recent seismological observations and mineral physics data. Importantly, there is a lack of quantitative comparison with the seismic data in these studies. Here we develop a model that includes fractional solidification and light-element segregation in an Fe alloy system, and invoke sedimentation of solid particles across the inner-outer core boundary. The liquidus and solidus phase diagram of an Fe-Si-O core are used as a model composition to understand the solidification and growth of the inner core. We infer that a compacting cumulate pile forms beneath the ICB (the *F'* layer). We examine the sound velocity-density profiles, grain size, permeability, residual porosity, and viscosity of an Fe alloy core across the ICB to explore the implications of the dynamical model. This scenario is consistent with mineral physics and seismological constraints at ICB conditions and provides a holistic model of inner-core growth.

2. Compositional Model of Earth's Core

The Earth's core is known to be composed of an Fe light-element alloy to balance its density deficit and velocity differences in seismic models compared to that of Fe-Ni alloy in mineral physics studies at relevant *P-T* conditions. Several light element candidates have been proposed, such as Si, O, S, C, and H (Poirier, 1994a), although which of these elements is the most abundant in the core is still a matter of intense debate (Li & Fei, 2014). The presence of a combination of these light elements is necessary to explain the density deficits and velocity discrepancies between pressure-density-velocity profiles of Fe and seismological observations (Hirose et al., 2013). Heretofore, many studies including comparison between high-pressure mineral physics data and seismic observations, Si isotope data, and geochemical models for core formation have supported Si being the most abundant light element present in the Earth's core (Allègre et al., 2001; Georg et al., 2007; Hirose et al., 2013; Lin et al., 2002; Mao et al., 2012; Zhang et al., 2016). Additionally, an O concentration less than 2.5 wt % in the liquid outer core is suggested by the experimentally measured density and sound velocity profiles of Fe-O system at the relevant *P-T* conditions of the core (Huang et al., 2011). Some of the proposed light elements have a very low solubility in Fe at ambient and high *P-T* conditions such as C and H (Li & Fei, 2014). Additionally, C and H have high volatility, so they are unlikely to be abundantly incorporated into Fe during differentiation and core formation (McDonough & Sun, 1995). S is a strong siderophile but moderately volatile element, whose geochemical and cosmochemical constraints give an upper limit of ~2 wt % S in the core through mass balance calculations of the bulk Earth compositions (Dreibus & Palme, 1996).

A density jump inferred from seismic data (~0.5–0.6 g/cm³) is present across the ICB (Dziewonski & Anderson, 1981; Kennett et al., 1995; Figure 2), which may be attributable to light-element release during crystallization. This suggests that the inner core contains approximately 30–50% less light elements than the outer core (Anderson & Isaak, 2002; Fei et al., 2016). Some theoretical calculations have suggested that O partitions more strongly from solid into liquid than Si and S (Alfè et al., 2002), so the solid inner core may be O poor upon freezing. High-pressure melting experiments of Fe-Si-O and Fe-S-O alloys in diamond anvil cells found that O could be left in the liquid upon freezing of the Fe alloys (Hirose et al., 2017; Yokoo et al., 2019). The Fe-Si-O alloy may crystallize SiO₂ as it cools so that O and Si would partition from solid to liquid

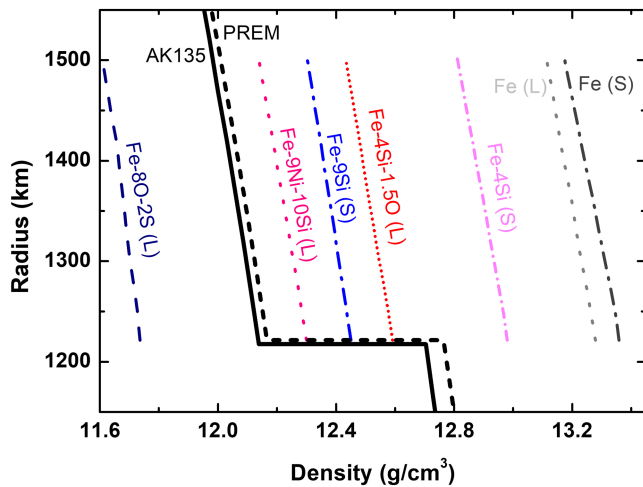


Figure 2. Densities of the Fe and Fe alloys as a function of depth near the inner-core boundary. Densities of liquid Fe-4Si-1.5O and solid Fe-4Si are higher than those of the outer core and the inner core, respectively, but their density contrast ($\sim 0.4 \text{ g/cm}^3$) is close to the AK135 and PREM models ($\sim 0.5\text{--}0.6 \text{ g/cm}^3$; Dziewonski & Anderson, 1981; Song & Helmberger, 1995). The symbols “L” and “S” represent the liquid and solid state, respectively. Densities at the relevant conditions of the ICB are shown for *hcp*-Fe (black dash-dotted line; Dewaele et al., 2006; Lin et al., 2005; Mao et al., 2012), liquid Fe (gray dashed line; Brown & McQueen, 1986; Ichikawa et al., 2014; Nguyen & Holmes, 2004), *hcp* Fe-9 wt % Si (blue dash-dotted line; Fischer et al., 2014), liquid Fe-9 wt % Ni-10 wt % Si (pink dotted line; Zhang et al., 2016), and liquid Fe-8 wt % O-2 wt % S (navy dashed line; Huang et al., 2011).

until one of the two is mostly depleted in the core (Hirose et al., 2017). Thus, a certain amount of O most likely exists in the liquid outer core but not in the inner core. Consequently, we adopt a compositional model for the Earth’s core where Fe-Si-O exists in the liquid outer core, while the solid inner core is mainly made of Fe-Si alloy. Experimental results on density, velocity, and a melting curve for the Fe-Si-O alloy are readily available for us to build our model. For the simplicity in the modeling, we do not include other light elements. However, we should note that this study does not exclude the coexistence of other light element(s).

The densities and sound velocities of Fe/Fe-Si/Fe-O alloys have been well investigated at the relevant conditions of Earth’s core (Huang et al., 2011; Lin et al., 2005; Mao et al., 2012; Zhang et al., 2016). Considering Si and O as the light elements in the outer core, a release of ~ 2 wt % O upon freezing would explain the density contrast of $\sim 4\%$ between the inner and outer core (Figure 2; Fischer et al., 2011; Huang et al., 2011). Comparison of the experimentally determined and modeled sound velocity of Fe and Fe-Si/Fe-O alloys with the PREM suggests a Si-rich Fe core with an outer core composition of $\sim 4\text{--}6$ wt % Si and $\sim 1\text{--}2.5$ wt % O, and an inner core of $\sim 4\text{--}6$ wt % Si (Hirose et al., 2013; Huang et al., 2011; Zhang et al., 2016; Figures 2–4).

Since Earth’s inner core solidifies across the ICB, a mixture of liquid and solid Fe light-element alloy is expected to co-exist at ICB conditions within the liquidus and solidus of the system (Figure 3a). Previous studies show that adding light elements such as Si, O, and S into Fe depresses its melting temperature (e.g., Fischer, 2016; Morard et al., 2014). For a given amount of light element in Fe, Fe-Si alloy has a higher melting temperature compared with Fe-O and Fe-S alloys so that Fe-Si would preferentially crystallize as the core cools (Huang et al., 2010; Mori et al., 2017; Zhang et al., 2018).

3. Solidification of Fe-Si-O System and Geodynamic Model

3.1. Solidification of Fe-Si-O System and Thermal Structure Across the ICB

To better understand the solidification and element partition processes and to build a plausible geodynamic model for the ICB, we investigated the *P-T* phase diagram of Fe-Si-O system from 313 to 329 GPa using literature results, corresponding to the radius of 1,500 to 1,220 km, respectively, in the *F* layer (Figure 3). Pure Fe has a single melting curve at high pressures, while a mixed core composition such as the ternary Fe-O-S/Fe-Si-S system has both a solidus and liquidus with a temperature gap (Fischer, 2016; Morard et al., 2014; Sakairi et al., 2017; Terasaki et al., 2011; Figure 3b). In our model, the core adiabat crosses the liquidus at the top of the *F* layer, while it is still higher than the solidus, as shown in Figure 3. As a result, the liquid starts to crystallize at the top of the *F* layer so a mixture of solid and liquid exists in the region. The temperature at the top of the *F* layer can be defined to be the liquidus temperature of Fe-Si-O alloy. Here, Fe-4 wt % Si-1.5 wt % O ($\text{Fe}_{87.7}\text{Si}_{7.4}\text{O}_{4.9}$ in atomic percent) is used for the outer core composition because its V_p displays velocity profiles similar to PREM data in the Earth’s outer core (Figure 4).

We modeled the solidus and liquidus of the Fe-Si-O alloy system at the relevant *P-T* conditions of the ICB using Matthiessen’s additive law based on recent laboratory data in Fe, Fe-Si, Fe-O, and Fe-Si-O systems (Figure S1 in the supporting information; Anzellini et al., 2013; Arveson et al., 2019; Fischer, 2016; Huang et al., 2010; Komabayashi, 2014; Komabayashi et al., 2019; Morard et al., 2014; Zhang et al., 2018). The solidus and liquidus for an Fe-4Si-1.5O (wt %) system used in this study are estimated to be $\sim 5,400$ and $\sim 5,550$ K at the top of the *F* layer from melting temperatures of an O-rich Fe alloy (e.g., Fe-8O-2S system (Huang et al., 2011)) and Si-rich Fe alloy (e.g., Fe-8Ni-10Si system and Fe-5Ni-4Si (Komabayashi et al., 2019; Zhang et al., 2018)) at ~ 313 GPa, respectively. Thus, the temperature at top of the *F* layer is $\sim 5,550$ K from the modeled liquidus temperature of Fe-4Si-1.5O.

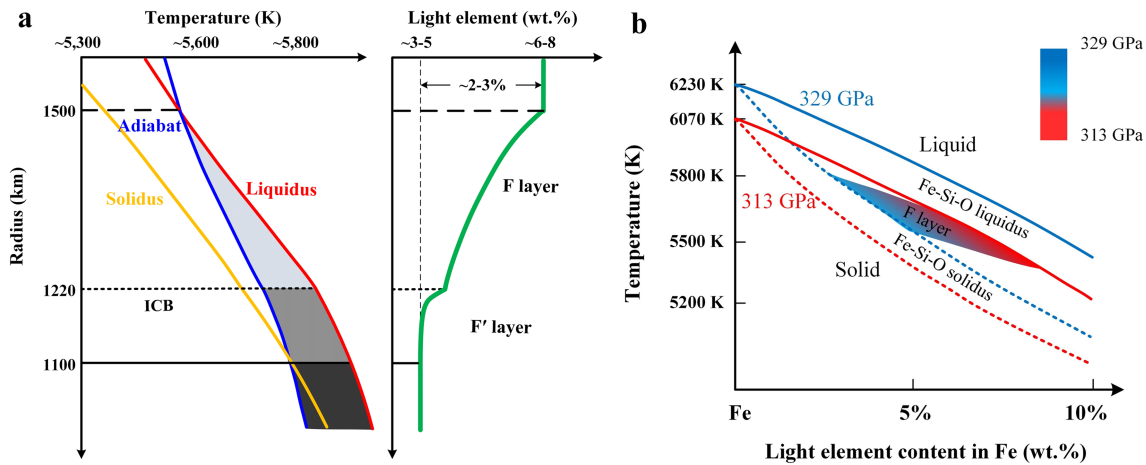


Figure 3. Thermal structure and phase diagram of Fe-Si-O system in the *F* and *F'* layer. (a) Schematic thermal structure and concentration of light elements across the inner-core boundary. In the left figure, red and orange lines represent the liquidus and solidus of Fe-Si-O alloy, respectively, and blue line shows the adiabat of Earth's core across the liquidus and solidus lines at the ICB. In the right figure, green line is the light element concentration of the core composition across the ICB. Horizontal dashed and dotted lines represent boundaries for the *F* and *F'* layers. (b) Solidus and liquidus of the Fe-Si-O system as a function of light element content in Fe at the relevant *P-T* conditions of the *F* layer. From the top (at ~313 GPa) to the bottom (at ~329 GPa) of the *F* layer, the adiabat temperature moves from Fe-Si-O liquidus close to solidus as shown in (a). The shaded area indicates the change of light element concentration under the conditions of the *F* layer, where the red gradually changing to blue represents a pressure gradient from 313 to 330 GPa (as shown in the color bar at the top right). We should note that the exact widths of the phase loops are not fully determined and will require refinements in the future. The solid upper line and dashed lower line represent the liquidus and the solidus as a function of the Si-O concentration at 313 GPa (red lines) and 329 GPa (blue lines), respectively.

At the ICB, most O partitions into the liquid due to the higher liquidus temperature of Fe-Si, so the temperature at the ICB is ~5,700 K from the modeled solidus temperature of Fe-4Si-1.5O (Figure S1; Huang et al., 2011; Komabayashi, 2014; Ozawa et al., 2011). The temperatures of the *F* layer are bracketed between the liquidus of the outer core composition and the solidus of the inner core composition, as shown in the shaded area of Figure 3b. The liquidus gradient of Fe alloy with a compositional gradient and the adiabat gradient in the *F* layer can be constrained linearly according to the phase diagram (Table 1).

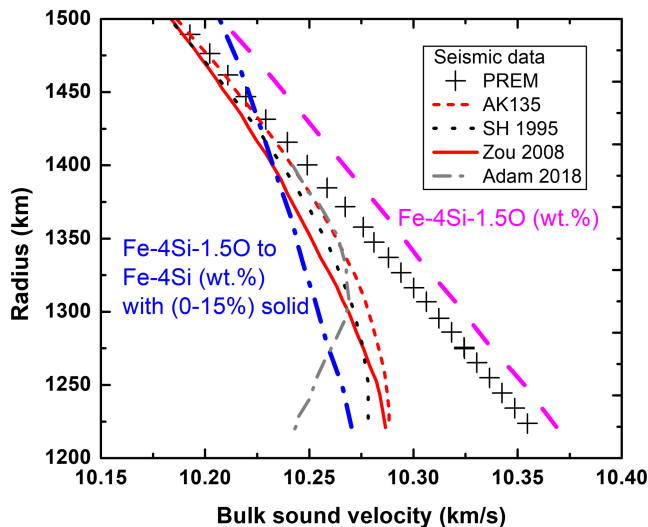


Figure 4. Compressional sound velocities of the Fe-Si-O slurry in the *F* layer compared with seismic data. The sound velocity of liquid Fe-4 wt % Si-1.5 wt % O generally matches with the PREM data in the outer core but is significantly faster than seismic profiles for the *F* layer reported in AK135 (Kennett et al., 1995) and Zou 2008 (Zou et al., 2008). Considering O partitioning between solid and liquid and its buoyant rise toward the top of the *F* layer, the composition of the layer gradually changes to Fe-4 wt % Si solid with a maximum of $15 \pm 5\%$ solid fraction toward the bottom of the *F* layer. The modeled sound velocity of the slurry, a mixture of Fe-4 wt % Si-1.5 wt % O liquid and Fe-4 wt % Si solid, generally matches the velocity profile reported by Zou et al. (2008).

3.2. Geodynamic Model Across the ICB

The cooling of Earth's core is a key factor in the crystallization process and the heat transfer in the core boundary layer. We build a geodynamic model to describe the solidification process of liquid Fe alloy across the ICB (Figure 5). The liquid core starts to crystallize when the temperature (adiabat) reaches the liquidus of the constituting Fe alloy. Although critical supercooling in the liquid Fe alloy at Earth's core pressures may be required for inner core nucleation (Huguet et al., 2018), the core grows by conductive cooling into the overlying mantle. The liquidus temperature of the Fe alloy increases with increasing depth (pressure) and with the accompanying decrease of the light element concentration. The temperature difference between the adiabat and liquidus steadily grows from the radius of 1,500 to 1,220 km, allowing for continuous solidification (Figure 3a). Although the process we propose is not adiabatic, consideration of a hypothetical core adiabat and its relationship with the core liquidus allows us to evaluate the potential for the formation of a slurry layer.

Sinking crystals are denser than the liquid due to the light element partitioning and the volume reduction caused by the phase change. This process results in a continuously stratified composition with light element concentration increasing toward the top of the *F* layer (Figure 3a, solid green line). Below the ICB, the adiabat temperature becomes close to

Table 1
Physical Parameters Used for the *F* and *F'* Layer Modeling in This Study

Physical parameters	Symbol	Value used
Density change across Fe alloy melting without any compositional change	$\Delta\rho$	0.10–0.15 g/cm ³
Pressure at the ICB	P_{ICB}	329 GPa
Pressure at the top of the <i>F</i> layer	P_F	313 GPa
Thickness of the <i>F</i> layer	D	280 km
Pressure gradient in the <i>F</i> layer	P'	-5.71×10^4 Pa/m
Latent heat of Fe alloy	L	500–750 kJ/kg ^a
Temperature at the ICB (from solidus of Fe-4Si-1.5O)	T_{ICB}	5,700 K
Temperature at the top of the <i>F</i> layer (from liquidus of Fe-4Si-1.5O)	T_F	5,550 K
Melting of Fe-4Si at the ICB	T_{m-ICB}	5,900 K
Adiabatic gradient	dT_a/dr	-0.5 (0.1) K/km
Liquidus gradient of the <i>F</i> layer (Fe-4Si-1.5O liquidus toward Fe-4Si liquidus)	dT_m/dr	-1.2 (0.2) K/km

Note. Our model uses a Si-rich Fe alloy as a composition of the Earth's core, including liquid Fe-4Si-1.5O and solid Fe-4Si as the main constituents of the outer and inner core, respectively.

^aThe values for the latent heats of Fe-light element alloys from literatures are 570 kJ/kg (Poirier, 1994b), 600 kJ/kg (Buffett et al., 1996), 625 kJ/kg (Nakagawa & Tackley, 2014), 660 kJ/kg (Labrosse, 2003), and 750 kJ/kg (Gubbins et al., 2011), respectively. Adiabatic gradient in the *F* layer (~280 km thick) is constrained based on the temperature gap between the top of the *F* layer and the ICB. Liquidus gradient in the *F* layer is approximately -1.2 K/km, where pressure and compositional change contribute about -0.5 K/km (Gubbins et al., 2008) and -0.7 K/km, respectively.

the solidus of the inner core, where most of the liquid solidifies and forms a liquid-solid boundary. Considering a ternary Fe-4Si-1.5O system as the composition of the Earth's outer core, Fe-Si crystallizes in the *F* layer so that O preferentially partitions from a solid into a liquid, forming a solid-liquid slurry (Figure 5). The released light element (oxygen) eventually rises into the liquid above the *F* layer. Solid Fe-4Si particles sink down and become more dominant proportion of the slurry layer, which may occur by grain growth and by an increase in the number of crystallizing particles. Eventually, a critical packing

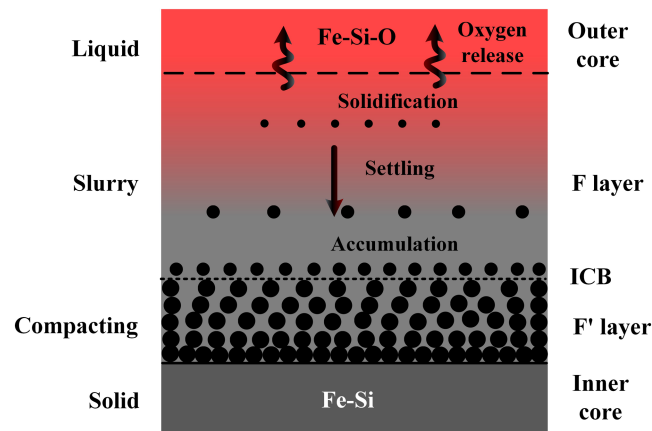


Figure 5. Schematic cartoon showing the solidification, element partitioning, and compaction of Fe alloy across the ICB. Liquid Fe-Si-O in the Earth's outer core crystallizes when its liquidus exceeds the adiabat at the top of the *F* layer as the core cools (Figure 2). During crystallization, oxygen preferentially partitions into liquid (Alfè et al., 2002; Hirose et al., 2017), forming Fe-Si solid particles and Fe-Si-O liquid. A mixture of solid-liquid phases exists as a result of crystal suspension in the *F* layer (slurry). Solid particles fall like snow and accumulate at the bottom of the *F* layer. A gradient of oxygen concentration is formed due to preferential partitioning, represented by red-gray scale shading where red and gray shadows indicate O distribution from rich to poor. At a radius of 1,500 km close to the top of the *F* layer, the concentration of the light elements is the same as the outer core (~6–8 wt %). At the bottom of the *F* layer (1,220 km), the composition is close to the inner core's (~3–5 wt %) as shown in Figure 3. Compaction occurs in the *F'* layer as a result of gravitational crystal accumulation. The material solidifies completely below the compacting cumulate *F'* layer. Solid circles show solid Fe-Si alloy particles.

fraction is reached where sinking crystals pile up at the bottom of the ICB, and the particles form a compacting cumulate pile (*F'* layer) below the *F* layer. Within the *F'* layer, the solid matrix continuously compacts under its own weight expelling trapped liquid Fe alloy into the *F* layer. Because the *F'* layer is supported by an interconnected network of solid particles, it exhibits some rigidity. Two important consequences of the compaction would be a density jump ($\Delta\rho$) and an increase in *P* wave velocity at the boundary between the *F* and *F'* layers because of the density and compositional difference between liquid and solid Fe alloys. The critical packing fraction at the boundary may be 50% to 70% according to studies of crystal accumulation in magma chambers (McKenzie, 2011). The compacting interface is still partially molten and is therefore permeable. The core becomes effectively solid below the base of the compacting pile, which contributes to the inner core's growth.

3.3. Solid Fraction in the *F* Layer

We examined the solid fraction in the *F* layer and compared the compressional sound velocity gradient for the slurry with seismic observations. To model the potential solid fraction in the *F* layer slurry as a function of radius, we use an equation for energy conservation described by Gubbins et al. (2008) and Malkus (1972):

$$\frac{df}{dr} = \frac{C_p}{L + P(\rho_p - \rho_f)} \frac{dT}{\rho_s^2 dr} \quad (1)$$

where C_p is the specific heat, L is the latent heat, dT is the temperature difference between the crystallized solid particles and the adjacent liquid, df is the difference of the liquid fraction, P is the pressure, and ρ_p and ρ_f are the densities of the solid and liquid alloys, which assumes adiabatic

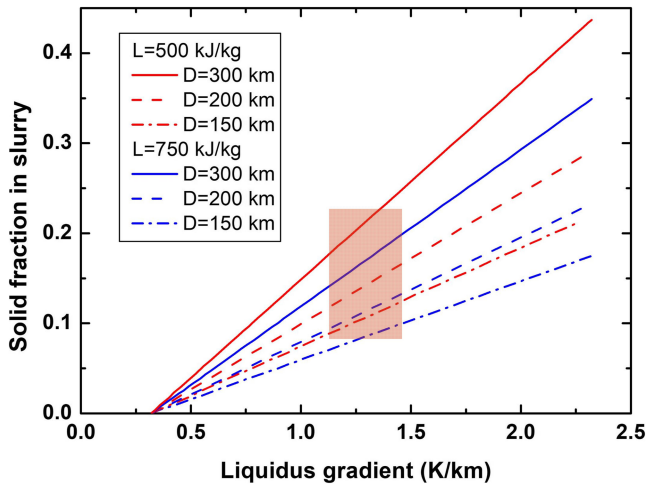


Figure 6. Solid fraction in the F layer slurry as a function of liquidus gradient, latent heat (“ L ”), and the thickness of the F layer (“ D ”), assuming adiabatic conditions. The solid fraction in the F layer has a positive relationship with the latent heat, the liquidus gradient of Fe alloy, and the thickness of the F layer. Taking a latent heat of 500–750 kJ/kg (Buffett et al., 1996; Gubbins et al., 2011; Labrosse, 2003; Nakagawa & Tackley, 2014; Poirier, 1994b) and a liquidus gradient of ~ 1.2 K/km for Fe alloy at an ~ 280 -km thickness of the F layer, we obtain a solid fraction of $\sim 15 \pm 5\%$ in the F layer slurry. The shadowed area represents the possible solid fraction at the F layer conditions.

conditions. The latent heat of the Fe-alloy crystallization at the ICB conditions is taken from 500 to 750 kJ/kg (Buffett et al., 1996; Gubbins et al., 2011; Labrosse, 2003; Nakagawa & Tackley, 2014; Poirier, 1994b). The other parameters used for the calculations are listed in Table 1. Within our model, solid particles fractionate from the slurry and solidification produces a compositional gradient in the liquid, deviating from adiabatic conditions. Even so, the simple adiabatic energy balance assumed in equation (1) demonstrates the potential for crystal fraction and variation with depth in the F layer slurry.

The calculated solid fraction as a function of the liquidus gradient, latent heat, and F layer thickness are shown in Figure 6. The liquidus gradient of Fe alloy with a compositional gradient across the F layer (e.g., Fe-4 wt % Si-1.5 wt % O liquidus toward close to Fe-4 wt % Si liquidus; dT_m/dr) is approximately -1.2 K/km, which is ~ 2 times higher than that estimated by Gubbins et al. (2008). They did not consider the potential increase in the melting temperature caused by light-element partitioning. For an ~ 280 -km-thick F layer, our model gives a solid fraction of about $15 \pm 5\%$ in the slurry. The solid fraction is much higher than previous estimates, which predicted a maximum solid fraction of 1–2% in the F layer (Gubbins et al., 2008).

3.4. Sound Velocity of Fe-Si-O Slurry in the F Layer

To investigate the reduced compressional-wave velocity in the F layer, the V_p of Fe-Si-O slurry was calculated based on previous experimental and/or modeled data of the densities and compressional sound velocities of hcp -Fe (Dewaele et al., 2006; Lin et al., 2005; Mao et al., 2012), liquid Fe (Brown & McQueen, 1986; Ichikawa et al., 2014; Nguyen & Holmes, 2004), hcp Fe-9 wt % Si (Fischer et al., 2014), liquid Fe-9 wt % Ni-10 wt % Si (Zhang et al., 2016), and liquid Fe-8 wt % O-2 wt % S (Huang et al., 2011) at the core conditions using the “Reuss average” model. The Reuss average model can effectively describe the sound velocity differences between pure liquid and two-phase suspension (slurry), as verified by ultrasonic measurements of the sound velocities for model suspensions and ice slurry (Langlois et al., 2011). The V_p was calculated using the equation:

$$\rho V_p^2 = K + \frac{4G}{3} \quad (2)$$

where ρ is the density and K and G are the bulk and shear moduli, respectively. In a slurry or liquid suspension, the shear modulus G approximately equals 0. So, we could obtain

$$V_{susp} = \sqrt{\frac{K_e}{\rho_e}} \quad (3)$$

where K_e is the effective elastic modulus of the two-phase slurry and ρ_e is the effective density.

$$\rho_e = \rho_p x_p + (1 - \rho_p) x_f \quad (4)$$

Moreover, K_e is obtained using Reuss average model here, which assumes uniform stress throughout the medium:

$$\frac{1}{K_e} = \frac{x_p}{K_p} + \frac{(1-x_p)}{K_f} \quad (5)$$

The V_p of Fe-4 wt % Si-1.5 wt % O generally matches the PREM of the outer core with a downward trend toward the top of the F layer (Figure 4; magenta dashed line), while it is significantly faster than the

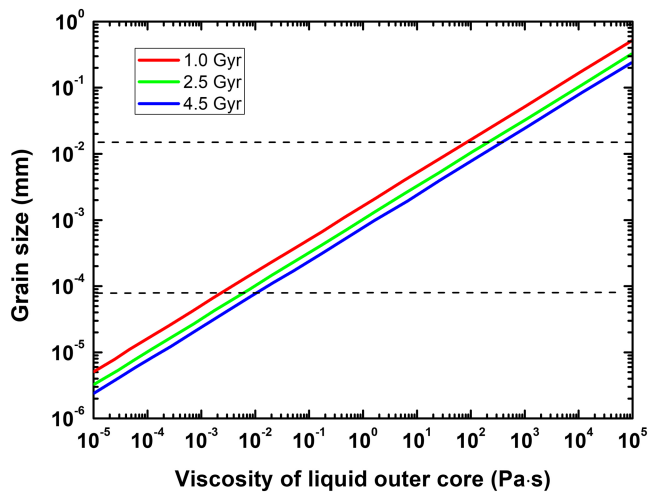


Figure 7. The calculated crystal grain size in the *F* layer as a function of the viscosity in the liquid outer core and inner-core age. The grain size has a log-linear relationship with the viscosity of liquid outer core. An estimated liquid outer-core viscosity of ~ 1 Pa/s gives a grain size of $\sim 10^{-3}$ mm in the slurry *F* layer. A younger inner core corresponds to larger crystal grain sizes in the *F* layer. Red, green, and blue solid lines represent the relations between the grain size in the *F* layer and the viscosity of liquid outer core at the inner-core age of 1.0, 2.5, and 4.5 Gyr, respectively.

AK135 and Zou 2008 models. When the liquid crystallizes and 1.5 wt % O gradually partitions into the liquid, the solid fraction of Fe-4 wt % Si particles ideally ranges from 0 to 15% toward the *F* layer bottom. The calculated V_p of the solid-liquid mixture is shown in Figure 4 (blue dash-dot line), which gradually decreases and matches the AK135, Zou 2008, and Adam 2018 models. Although there are uncertainties both in the mineral physics data and seismic profiles, their overall trends are consistent with each other.

The compacting cumulate pile that forms the boundary between the inner and outer core occurs when the packing fraction reaches up to ~ 50 – 70% due to solid particle accumulation at the bottom of the *F* layer. The clast-supported framework induces rigidity, transferring the Fe alloy slurry from liquid-like to solid-like (Cates et al., 1998). This transition would produce a sharp increase in seismic velocity as seen at the ICB because of the change in wave-carrying phase from liquid to a phase with nonzero shear modulus. Analogous behavior has been observed in ultrasonic experiments on ice slurry (Langlois et al., 2011) and some dense suspensions (Han et al., 2016).

3.5. Particle Grain Size in the *F* Layer

Our model requires continuous solidification and sinking of crystals in the *F* layer. Inner core growth rate places an important constraint on possible accumulation rates and hence the grain size of the Fe alloy snowing in the *F* layer. We investigated the grain size of solid crystals in the liquid *F* layer

implied by several possible inner-core growth rates (1.22, 0.49, and 0.27 mm/year, corresponding to the inner-core age of 1.0, 2.5, and 4.5 Gyr, respectively), which were calculated as a function of the viscosity of the liquid outer core using Stokes' law:

$$r = \sqrt{\frac{9v\eta_f}{2\Delta\rho g}} \quad (6)$$

where r is the sinking particle radius, v is the effective velocity of the sinking particles (estimated using the inner-core growth rates scaled by the solid fraction in the *F* layer), η_f is the viscosity of the outer core liquid, g is the gravitational acceleration (4.40 m/s² at the ICB), and $\Delta\rho$ is the density difference between solid and liquid. The crystal grain size and liquid outer-core viscosity have a log-linear relationship as shown in Figure 7. Previous studies argue that the viscosity of the fluid outer core (η_f) is between 10^{-2} and 10^2 Pa/s (de Wijs et al., 1998; Desgranges & Delhommelle, 2007; Palmer & Smylie, 2005; Smylie et al., 2009), corresponding to effective grain radii between 10^{-4} and 10^{-2} mm, respectively. If we assume the outer core viscosity as ~ 1 Pa/s and a younger inner core of ~ 1.0 Gyr recently claimed (Davies et al., 2015), the grain size in the *F* layer is $\sim 10^{-3}$ mm at the *F* layer conditions (Figure 7). A study of the entrainment of sediments in convecting liquids suggests that particles larger than 3×10^{-5} – 10^{-4} mm would not be entrained by the outer-core thermal convection (Solomatov et al., 1993), indicating that the grain sizes implied by our model would successfully sink to form the inner core for any of the core growth rates we investigated.

3.6. Residual Porosity and Permeability in the *F*' Layer

Accumulating solid particles form a cumulate pile at the bottom of the ICB, the *F*' layer, which compacts under its own weight, squeezing liquid into the overlying slurry (*F* layer) and outer core. A secondary layer of “residual porosity” may exist *beneath* the primary compacting region (i.e., within the inner core) depending on the sedimentation velocity, fluid viscosity, and permeability (e.g., Shirley, 1986; Sumita et al., 1996). We may estimate the residual porosity (ϕ_r) beneath the *F*' layer, which is proportional to

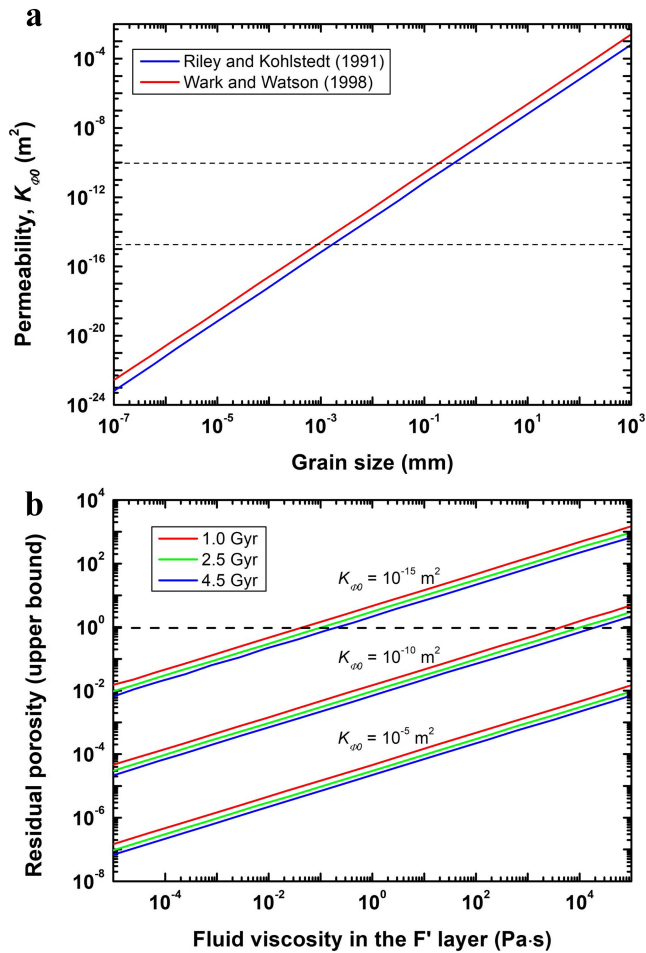


Figure 8. Estimated permeability at the F - F' layer boundary and residual porosity beneath the compacting cumulate pile (F' layer). (a) Reference permeability calculated as a function of grain size in the compacting pile using models of Wark and Watson (1998) (red line) and Riley and Kohlstedt (1991) (blue line), assuming a fluid fraction of 50%. (b) Residual porosity beneath the F' layer as a function of fluid viscosity calculated assuming no solidification in the inner core. The residual porosities were calculated at permeabilities of 10^{-5} , 10^{-10} , and 10^{-15} m^2 , respectively, and at the inner-core ages of 1.0 Gyr (red line), 2.5 Gyr (green line), and 4.5 Gyr (blue line). At a permeability of $\sim 10^{-10}$ m^2 , the residual porosity is approximately 10^{-2} for the fluid viscosities of ~ 1 Pa/s. Because continuous solidification in the F' layer must occur, these residual porosity calculations represent upper bounds.

indicating a larger heat flux out of the core at the western CMB (Aubert et al., 2008). Inhomogeneous physical and chemical conditions at the base of the mantle, including postperovskite transition in the D'' layer and iron chemistry-related thermal conductivity, can also produce lateral variation in the CMB heat flux of approximately 10–50% (Ammann et al., 2014; Romanowicz & Gung, 2002; Van der Hilst et al., 2007). As a result, heat flux variations on the ICB may be expected because of spatial variations in heat flux to the overlying mantle (Gubbins et al., 2011). Recent numerical simulations of the dynamics of the fluid core indicate that there exists heterogeneous core-mantle boundary heat flux, which could cause regional thermal inversion layers extending hundreds of kilometers into the outer core. Specifically, the CMB heat flux in African and Pacific LLSVPs (Large Low Shear Velocity Provinces) is lower than other locations, producing uneven inner-core growth (Mound et al., 2019). The temperature variation at the base of the mantle and the heat flux variation across the core is critical in determining the growth rate of the F and F' layers. As a result of these

$$\phi_r = \sqrt{\frac{\phi_0^3 \eta_f V_0}{K_{\phi_0} (1 - \phi_0) \Delta \rho g}} \quad (7)$$

where ϕ_0 is the porosity at the critical packing fraction (0.5), η_f is the viscosity of the fluid, V_0 is the settling velocity, K_{ϕ_0} is the reference permeability, $\Delta \rho$ is the density difference between solid and liquid, and g is the gravitational acceleration at the ICB (Sumita et al., 1996).

Because the sedimentation velocity is constrained by the core growth rate and core fluid viscosity is thought to be relatively low (de Wijs et al., 1998; Desgranges & Delhommelle, 2007; Palmer & Smylie, 2005; Smylie et al., 2009), within our model residual porosity mainly depends on the permeability, which varies with grain size (e.g., Riley & Kohlstedt, 1991; Wark & Watson, 1998). Low permeabilities at the inner-core boundary (i.e., $< 10^{-13}$ m^2) imply an appreciable residual porosity (volume of liquid) in the inner core (see equation (7)), which is not supported by seismic observations (Deguen et al., 2007).

In Figure 8a, we present reference permeabilities for the F' layer as a function of grain radius assuming a critical packing fraction of $\sim 50\%$, using permeability models of Riley and Kohlstedt (1991) and Wark and Watson (1998). For grain sizes implied by reasonable inner core growth rates and fluid viscosities (10^{-4} to 10^{-2} mm; see section 3.5), permeability is low ($< 10^{-13}$ m^2). Residual porosities are shown in Figure 8b as a function of permeability and fluid viscosity. We expect grain size of solid particles in the F' layer to be larger than those in the F layer because of continuous grain growth owing to (1) annealing and (2) continued solidification in the F' layer. Assuming F' layer grain sizes of size of 10^{-3} to 10^{-1} mm implies F' permeabilities between 10^{-13} and 10^{-10} m^2 . Because grain size is expected to increase in the F' layer, residual porosities shown in Figure 9b should be considered as upper bounds. For fluid viscosities between 10^{-2} and 10^2 Pa/s, the implied upper bound residual porosity is 1% to 15% for a permeability of 10^{-10} m^2 in the F' layer, suggesting an inner core with a vanishingly small residual porosity.

4. Discussions and Implications

4.1. Hemispheric Asymmetry in the F' Layer

Previous studies have shown that cold deep subducted lithospheres, such as that beneath Central America (in the western hemisphere; Van der Hilst et al., 2007; van der Hilst et al., 1997), can extract more heat from the core than warm thermochemical piles, such as that beneath the central Pacific (in the eastern hemisphere; McNamara & Zhong, 2005), indicating

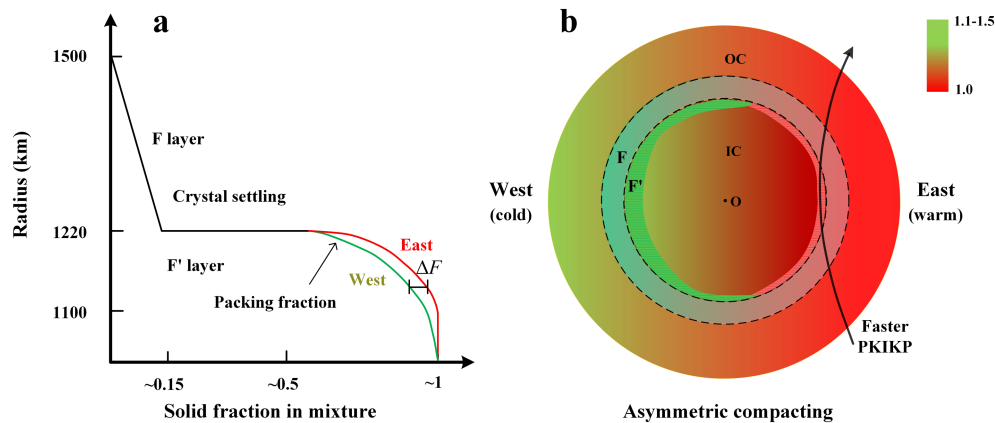


Figure 9. Asymmetric solidification and compaction between the eastern and western hemispheres near the inner-core boundary. The radius versus solid fraction in the Fe alloy solid-liquid mixture phase across the ICB (a) and one-dimensional heat flux across the ICB (color contours, where the western hemisphere core in green has approximately 10–50% greater heat flux than that of the eastern hemisphere in red) on the equatorial section of the core (b). The east side is warmer than the west side around the base of the mantle (Aubert et al., 2008; Khan et al., 2008; McNamara & Zhong, 2005; Nakagawa & Tackley, 2008; Van der Hilst et al., 2007), which likely causes the hemispheric asymmetry in the thickness of the F' layer. The eastern hemisphere of the inner core has a thinner compacting thickness (~100 km) with a faster seismic wave velocity than the western hemisphere (~200 km). ΔF is the solid fraction difference between the west (green curve) and east (red curve) hemispheres in the F' layer.

variations, solidification around the ICB may not be homogeneous (supporting information), producing a variation in the thickness of the compacting F' layer (shown schematically in Figure 9).

The solid fraction in the F' layer increases from the critical value (50–70%) to nearly 100% with continuous solidification and compaction (Figure 9a). Specifically, the relatively higher heat flux in the cold western hemisphere would hasten solidification around the ICB, so the western hemisphere has a higher sedimentation rate (Tkalcic, 2015). Correspondingly, the greater sedimentation rate could result in a thicker compacting pile (Sumita et al., 1996). We, therefore, argue that Earth's western hemisphere has a thicker compacting layer (F' layer) than the eastern hemisphere on average (Figure 9b). Consequently, at the same radius in the F' layer, a thin compacting pile in the eastern hemisphere would have a higher solid fraction (Figure 9a), which could cause a faster sound velocity consistent with seismic observations (Figure 9b; Monnereau et al., 2010).

Seismic studies have shown that the P wave velocity asymmetry between the two hemispheres at the top ~100 km of the F' layer (~1.5%) is much larger than that at its deeper parts (~0.5%; Figure 1; Deuss, 2014; Yu & Wen, 2006). This can be explained by variations of the compacting F' layer thickness. At the top ~100 km, the solid fraction difference (ΔF) between the two hemispheres could produce P wave velocity asymmetry (Figure 9a). With a mostly solidified eastern hemisphere (such as that below ~150 km of the ICB), the ΔF would decrease with increasing depth, resulting in the diminution of the P wave asymmetry between the two hemispheres.

4.2. Estimated Shear Viscosity of the Inner Core

Interpreting the F' layer as a compacting cumulate pile allows us to estimate the shear viscosity of the solid in the layer. Sumita et al. (1996) conducted a linear analysis to isolate physical controls on the thickness and porosity of the compacting pile. They found that in cases where the rate of particle sedimentation is much less than the Darcy velocity for fluid expelled from the compacting medium (i.e., our F' layer), the layer thickness (D') can be described by

$$D' = \sqrt{\frac{4\eta_s}{3(\rho_s - \rho_l)g}} V_0 \quad (8)$$

where η_s is the shear viscosity of the solid, g is the gravitational constant, V_0 is the sedimentation (settling) rate, and ρ_s and ρ_l are the densities of the solid and liquid alloys, respectively. Because the F' layer thickness

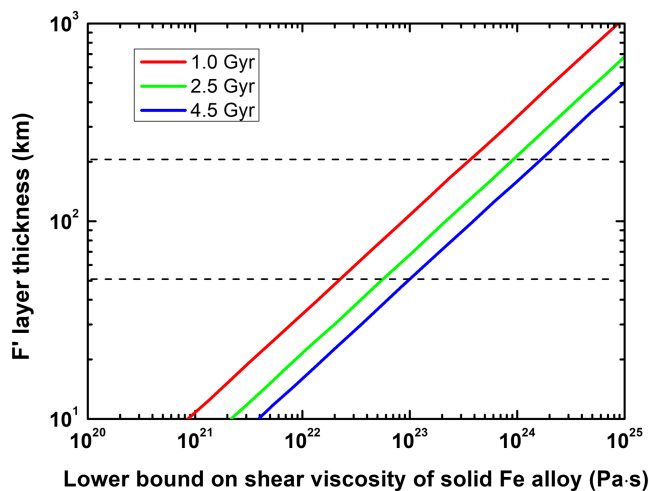


Figure 10. Lower bound on shear viscosity of solid Fe alloy in a quasi-steady state F' layer versus the F' layer thickness for different inner-core ages. The calculated shear viscosity assumes no solidification within the F' layer and has a log-linear relationship with F' layer thickness. A younger inner core corresponds to a lower shear viscosity of solid Fe alloy. The F' layer has a thickness of ~ 50 – 200 km in seismic observations, suggesting a shear viscosity $>10^{22}$ Pa/s in the solid inner core. Red, green, and blue solid lines represent the relations between the F' layer thickness and the shear viscosity of solid Fe alloy at the inner-core age of 1.0, 2.5, and 4.5 Gyr, respectively.

5. Conclusions

Our model for the F and F' layers provides a simple and reasonable explanation for the observed seismic gradient and hemispheric asymmetry. Inner core growth happens as a result of the secular cooling of the outer core when the core adiabat cools below the liquidus of Fe-Si-O system. An Fe-Si-O slurry with approximately 15% Fe-Si solid particles occurs when the core temperature decreases below the liquidus of Fe-Si-O, causing a compositional gradient with depth in the lowermost outer core. Crystallization of liquid Fe-Si-O alloy with light element partitioning (e.g., O) can cause a gradually reduced seismic velocity in the F layer, consistent with recent seismic observations. A compacting cumulate pile forms at the lower part of the ICB as a result of the accumulation of solid particles extending to the top of the F' layer, where residual liquid is continuously expelled into the F layer. Lateral variations of the cumulate pile thickness at the upper inner core induce west-east asymmetry in P wave velocity. Consideration of seismic observations within the dynamic model framework provides additional details on particle grain size in the F layer, permeability, shear viscosity, and residual porosity in the inner core. The segregation of light element-enriched liquid and the latent heat of Fe alloy solidification across the ICB can play an important role in driving compositional convection of the outer core, powering Earth's magnetic fields (Driscoll & Bercovici, 2014; Nimmo, 2015).

Acknowledgments

We thank Bruce A. Buffett for the constructive comments that improved this manuscript. Thanks to Frejja O'Toole who read our manuscript and made editorial suggestions. Y.Z. acknowledges supports from the National Natural Science Foundation of China (grant 41804082) and the Fundamental Research Funds for the Central Universities (YJ201809). N.D. acknowledges support of a postdoctoral fellowship provided by the Jackson School of Geosciences, the University of Texas at Austin. J.-F.L. acknowledges supports from the Geophysics Program of the National Science Foundation (NSF EAR-1901801) and Deep Carbon Observatory of the Sloan Foundation.

References

- Adam, J.-C., Ibourichène, A., & Romanowicz, B. (2018). Observation of core sensitive phases: Constraints on the velocity and attenuation profile in the vicinity of the inner-core boundary. *Physics of the Earth and Planetary Interiors*, 275, 19–31.
- Alboussière, T., Deguen, R., & Melzani, M. (2010). Melting-induced stratification above the Earth's inner core due to convective translation. *Nature*, 466(7307), 744–747.
- Alfè, D., Gillan, M. J., & Price, G. D. (2002). Composition and temperature of the Earth's core constrained by combining ab initio calculations and seismic data. *Earth and Planetary Science Letters*, 195(1–2), 91–98.
- Allègre, C., Manhès, G., & Lewin, É. (2001). Chemical composition of the Earth and the volatility control on planetary genetics. *Earth and Planetary Science Letters*, 185(1), 49–69.
- Ammann, M. W., Walker, A. M., Stackhouse, S., Wookey, J., Forte, A. M., Brodholt, J. P., & Dobson, D. P. (2014). Variation of thermal conductivity and heat flux at the Earth's core mantle boundary. *Earth and Planetary Science Letters*, 390, 175–185.
- Anderson, O., & Isaak, D. (2002). Another look at the core density deficit of Earth's outer core. *Physics of the Earth and Planetary Interiors*, 131(1), 19–27.
- Anzellini, S., Dewaele, A., Mezouar, M., Loubeyre, P., & Morard, G. (2013). Melting of iron at Earth's inner core boundary based on fast X-ray diffraction. *Science*, 340(6131), 464–466.
- Arveson, S. M., Deng, J., Karki, B. B., & Lee, K. K. M. (2019). Evidence for Fe-Si-O liquid immiscibility at deep Earth pressures. *Proceedings of the National Academy of Sciences of the United States of America*, 116(21), 10,238–10,243. <https://doi.org/10.1073/pnas.1821712116>

- Aubert, J., Amit, H., Hulot, G., & Olson, P. (2008). Thermochemical flows couple the Earth's inner core growth to mantle heterogeneity. *Nature*, *454*(7205), 758–761.
- Braginskii, S. I. (1963). The structure of the *F* layer and the reasons for convection in the earth core. *Dokl. Akad. Nauk SSSR*, *149*(6), 1311–1314.
- Breuer, D., Rueckriemen, T., & Spohn, T. (2015). Iron snow, crystal floats, and inner-core growth: modes of core solidification and implications for dynamos in terrestrial planets and moons. *Progress in Earth and Planetary Science*, *2*(1), 39.
- Brown, J. M., & McQueen, R. G. (1986). Phase transitions, Grüneisen parameter, and elasticity for shocked iron between 77 GPa and 400 GPa. *Journal of Geophysical Research*, *91*(B7), 7485–7494.
- Buffett, B. A. (1997). Geodynamic estimates of the viscosity of the Earth's inner core. *Nature*, *388*(6642), 571–573.
- Buffett, B. A. (2000). Earth's core and the geodynamo. *Science*, *288*(5473), 2007–2012. <https://doi.org/10.1126/science.288.5473.2007>
- Buffett, B. A., Garnero, E. J., & Jeanloz, R. (2000). Sediments at the Top of Earth's Core. *Science*, *290*(5495), 1338–1342.
- Buffett, B. A., Huppert, H. E., Lister, J. R., & Woods, A. W. (1996). On the thermal evolution of the Earth's core. *Journal of Geophysical Research*, *101*(B4), 7989–8006.
- Cates, M., Wittmer, J., Bouchaud, J.-P., & Claudin, P. (1998). Jamming, force chains, and fragile matter. *Physical Review Letters*, *81*(9), 1841–1844.
- Cormier, V. F., Attanayake, J., & He, K. (2011). Inner core freezing and melting: Constraints from seismic body waves. *Physics of the Earth and Planetary Interiors*, *188*(3), 163–172.
- Davies, C., Pozzo, M., Gubbins, D., & Alfe, D. (2015). Constraints from material properties on the dynamics and evolution of Earth's core. *Nature Geoscience*, *8*(9), 678–685.
- Davies, C. J., & Pommier, A. (2018). Iron snow in the Martian core? *Earth and Planetary Science Letters*, *481*(Supplement C), 189–200.
- de Wijs, G. A., Kresse, G., Vočadlo, L., Dobson, D., Alfe, D., Gillan, M. J., & Price, G. D. (1998). The viscosity of liquid iron at the physical conditions of the Earth's core. *Nature*, *392*(6678), 805–807.
- Deguen, R. (2012). Structure and dynamics of Earth's inner core. *Earth and Planetary Science Letters*, *333*, 211–225.
- Deguen, R., Alboussière, T., & Brito, D. (2007). On the existence and structure of a mush at the inner core boundary of the Earth. *Physics of the Earth and Planetary Interiors*, *164*(1), 36–49.
- Desgranges, C., & Delhommelle, J. (2007). Viscosity of liquid iron under high pressure and high temperature: Equilibrium and nonequilibrium molecular dynamics simulation studies. *Physical Review B*, *76*(17), 172102.
- Deuss, A. (2014). Heterogeneity and anisotropy of Earth's inner core. *Annual Review of Earth and Planetary Sciences*, *42*, 103–126.
- Deuss, A., Irving, J. C., & Woodhouse, J. H. (2010). Regional variation of inner core anisotropy from seismic normal mode observations. *Science*, *328*(5981), 1018–1020. <https://doi.org/10.1126/science.1188596>
- Dewaele, A., Loubeyre, P., Occelli, F., Mezouar, M., Dorogokupets, P. I., & Torrent, M. (2006). Quasihydrostatic equation of state of iron above 2 Mbar. *Physical Review Letters*, *97*(21), 215504. <https://doi.org/10.1103/PhysRevLett.97.215504>
- Dreibus, G., & Palme, H. (1996). Cosmochemical constraints on the sulfur content in the Earth's core. *Geochimica et Cosmochimica Acta*, *60*(7), 1125–1130.
- Driscoll, P., & Bercovici, D. (2014). On the thermal and magnetic histories of Earth and Venus: Influences of melting, radioactivity, and conductivity. *Physics of the Earth and Planetary Interiors*, *236*, 36–51.
- Dziewonski, A. M., & Anderson, D. L. (1981). Preliminary reference Earth model. *Physics of the Earth and Planetary Interiors*, *25*(4), 297–356.
- Fearn, D. R., Loper, D. E., & Roberts, P. H. (1981). Structure of the Earth's inner core. *Nature*, *292*(5820), 232–233.
- Fei, Y., Murphy, C., Shibasaki, Y., Shahar, A., & Huang, H. (2016). Thermal equation of state of hcp-iron: Constraint on the density deficit of Earth's solid inner core. *Geophysical Research Letters*, *43*, 6837–6843. <https://doi.org/10.1002/2016GL069456>
- Fischer, R. A. (2016). Melting of Fe Alloys and the Thermal Structure of the Core. In H. Terasaki, & R. A. Fischer (Eds.), *Deep Earth: Physics and Chemistry of the Lower Mantle and Core* (pp. 1–12). Hoboken, NJ: Inc: John Wiley & Sons.
- Fischer, R. A., Campbell, A. J., Caracas, R., Reaman, D. M., Heinz, D. L., Dera, P., & Prakapenka, V. B. (2014). Equations of state in the Fe–FeSi system at high pressures and temperatures. *Journal of Geophysical Research: Solid Earth*, *119*, 2810–2827.
- Fischer, R. A., Campbell, A. J., Shofner, G. A., Lord, O. T., Dera, P., & Prakapenka, V. B. (2011). Equation of state and phase diagram of FeO. *Earth and Planetary Science Letters*, *304*(3), 496–502.
- Georg, R. B., Halliday, A. N., Schauble, E. A., & Reynolds, B. C. (2007). Silicon in the Earth's core. *Nature*, *447*(7148), 1102–1106.
- Gubbins, D., Masters, G., & Nimmo, F. (2008). A thermochemical boundary layer at the base of Earth's outer core and independent estimate of core heat flux. *Geophysical Journal International*, *174*(3), 1007–1018.
- Gubbins, D., Sreenivasan, B., Mound, J., & Rost, S. (2011). Melting of the Earth's inner core. *Nature*, *473*(7347), 361–363. <https://doi.org/10.1038/nature10068>
- Han, E., Peters, I. R., & Jaeger, H. M. (2016). High-speed ultrasound imaging in dense suspensions reveals impact-activated solidification due to dynamic shear jamming. *Nature Communications*, *7*, 12243.
- Hirose, K., Labrosse, S., & Hernlund, J. (2013). Composition and State of the Core. *Annual Review of Earth and Planetary Sciences*, *41*, 657–691.
- Hirose, K., Morard, G., Sinmyo, R., Umemoto, K., Hernlund, J., Helffrich, G., & Labrosse, S. (2017). Crystallization of silicon dioxide and compositional evolution of the Earth's core. *Nature*, *543*(7643), 99–102. <https://doi.org/10.1038/nature21367>
- Huang, H., Fei, Y., Cai, L., Jing, F., Hu, X., Xie, H., et al. (2011). Evidence for an oxygen-depleted liquid outer core of the Earth. *Nature*, *479*(7374), 513–516. <https://doi.org/10.1038/nature10621>
- Huang, H., Hu, X., Jing, F., Cai, L., Shen, Q., Gong, Z., & Liu, H. (2010). Melting behavior of Fe–O–S at high pressure: A discussion on the melting depression induced by O and S. *Journal of Geophysical Research*, *115*, B05207. <https://doi.org/10.1029/2009JB006514>
- Huguet, L., Van Orman, J. A., Hauck, S. A., & Willard, M. A. (2018). Earth's inner core nucleation paradox. *Earth and Planetary Science Letters*, *487*, 9–20.
- Ichikawa, H., Tsuchiya, T., & Tange, Y. (2014). The P–V–T equation of state and thermodynamic properties of liquid iron. *Journal of Geophysical Research: Solid Earth*, *119*, 240–252.
- Kennett, B., Engdahl, E., & Buland, R. (1995). Constraints on seismic velocities in the Earth from traveltimes. *Geophysical Journal International*, *122*(1), 108–124.
- Khan, A., Connolly, J., & Taylor, S. (2008). Inversion of seismic and geodetic data for the major element chemistry and temperature of the Earth's mantle. *Journal of Geophysical Research*, *113*, B09308. <https://doi.org/10.1029/2007JB005239>
- Komabayashi, T. (2014). Thermodynamics of melting relations in the system Fe–FeO at high pressure: Implications for oxygen in the Earth's core. *Journal of Geophysical Research: Solid Earth*, *119*, 4164–4177.

- Komabayashi, T., Pesce, G., Sinmyo, R., Kawazoe, T., Breton, H., Shimoyama, Y., et al. (2019). Phase relations in the system Fe–Ni–Si to 200 GPa and 3900 K and implications for Earth's core. *Earth and Planetary Science Letters*, *512*, 83–88.
- Labrosse, S. (2003). Thermal and magnetic evolution of the Earth's core. *Physics of the Earth and Planetary Interiors*, *140*(1-3), 127–143.
- Langlois, V., Gautherin, W., Laurent, J., Royon, L., Fournaison, L., Delahaye, A., & Jia, X. (2011). Ultrasonic determination of the particle concentration in model suspensions and ice slurry. *International Journal of Refrigeration*, *34*(8), 1972–1979.
- Li, J., & Fei, Y. (2014). Experimental Constraints on Core Composition. In K. K. Turekian (Ed.), *Treat. Geochem.* (pp. 527–557). Oxford: Elsevier.
- Lin, J.-F., Heinz, D. L., Campbell, A. J., Devine, J. M., & Shen, G. (2002). Iron-silicon alloy in Earth's core? *Science*, *295*(5553), 313–315.
- Lin, J.-F., Sturhahn, W., Zhao, J., Shen, G., Mao, H. K., & Hemley, R. J. (2005). Sound Velocities of Hot Dense Iron: Birch's Law Revisited. *Science*, *308*(5730), 1892–1894. <https://doi.org/10.1126/science.1111724>
- Loper, D. E. (1983). Structure of the inner core boundary. *Geophysical & Astrophysical Fluid Dynamics*, *25*(1-2), 139–155.
- Loper, D. E., & Roberts, P. H. (1977). On the motion of an iron-alloy core containing a slurry: I. general theory. *Geophysical & Astrophysical Fluid Dynamics*, *9*(1), 289–321.
- Loper, D. E., & Roberts, P. H. (1980). On the motion of an iron-alloy core containing a slurry. II. A simple model. *Geophysical & Astrophysical Fluid Dynamics*, *16*(1), 83–127.
- Loper, D. E., & Roberts, P. H. (1981). A study of conditions at the inner core boundary of the earth. *Physics of the Earth and Planetary Interiors*, *24*(4), 302–307.
- Malkus, V. R. W. (1972). Convection at the melting point: A thermal history of the earth's core. *Geophysical Fluid Dynamic*, *4*(1), 267–278.
- Mao, Z., Lin, J.-F., Liu, J., Alatas, A., Gao, L., Zhao, J., & Mao, H.-K. (2012). Sound velocities of Fe and Fe-Si alloy in the Earth's core. *Proceedings in National Academy Science USA*, *109*(26), 10,239–10,244.
- McDonough, W. F., & Sun, S.-S. (1995). The composition of the Earth. *Chemical Geology*, *120*(3), 223–253.
- McKenzie, D. (2011). Compaction and Crystallization in Magma Chambers: Towards a Model of the Skaergaard Intrusion. *Journal of Petroleum*, *52*(5), 905–930.
- McNamara, A. K., & Zhong, S. (2005). Thermochemical structures beneath Africa and the Pacific Ocean. *Nature*, *437*(7062), 1136–1139. <https://doi.org/10.1038/nature04066>
- Monnereau, M., Calvet, M., Margerin, L., & Souriau, A. (2010). Lopsided growth of Earth's inner core. *Science*, *328*(5981), 1014–1017.
- Morard, G., Andrault, D., Antonangeli, D., & Bouchet, J. (2014). Properties of iron alloys under the Earth's core conditions. *C. R. Geosci.*, *346*(5), 130–139.
- Mori, Y., Ozawa, H., Hirose, K., Sinmyo, R., Tateno, S., Morard, G., & Ohishi, Y. (2017). Melting experiments on Fe–Fe₃S system to 254 GPa. *Earth and Planetary Science Letters*, *464*, 135–141.
- Mound, J., Davies, C., Rost, S., & Aurnou, J. (2019). Regional stratification at the top of Earth's core due to core–mantle boundary heat flux variations. *Nature Geoscience*, *12*(7), 575–580.
- Nakagawa, T., & Tackley, P. J. (2008). Lateral variations in CMB heat flux and deep mantle seismic velocity caused by a thermal–chemical–phase boundary layer in 3D spherical convection. *Earth and Planetary Science Letters*, *271*(1), 348–358.
- Nakagawa, T., & Tackley, P. J. (2014). Influence of combined primordial layering and recycled MORB on the coupled thermal evolution of Earth's mantle and core. *Geochemistry Geophysics Geosystems*, *15*(3), 619–633.
- Nguyen, J. H., & Holmes, N. C. (2004). Melting of iron at the physical conditions of the Earth's core. *Nature*, *427*(6972), 339–342. <https://doi.org/10.1038/nature02248>
- Nimmo, F. (2015). Energetics of the Core. In G. Schubert (Ed.), *Treat Geophysical*, (Vol. 8, pp. 27–55). Oxford: Elsevier.
- Niu, F., & Wen, L. (2001). Hemispherical variations in seismic velocity at the top of the Earth's inner core. *Nature*, *410*(6832), 1081–1084.
- Ohta, K., Kuwayama, Y., Hirose, K., Shimizu, K., & Ohishi, Y. (2016). Experimental determination of the electrical resistivity of iron at Earth's core conditions. *Nature*, *534*(7605), 95–98. <https://doi.org/10.1038/nature17957>
- Ohtaki, T., & Kaneshima, S. (2015). Independent estimate of velocity structure of Earth's lowermost outer core beneath the northeast Pacific from PKiKP–PKPbc differential traveltimes and dispersion in PKPbc. *Journal of Geophysical Research: Solid Earth*, *120*, 7572–7586.
- Ozawa, H., Takahashi, F., Hirose, K., Ohishi, Y., & Hirao, N. (2011). Phase Transition of FeO and Stratification in Earth's Outer Core. *Science*, *334*(6057), 792–794.
- Palmer, A., & Smylie, D. (2005). VLBI observations of free core nutations and viscosity at the top of the core. *Physics of the Earth and Planetary Interiors*, *148*(2-4), 285–301.
- Poirier, J.-P. (1994a). Light elements in the Earth's outer core: A critical review. *Physics of the Earth and Planetary Interiors*, *85*(3), 319–337.
- Poirier, J.-P. (1994b). Physical properties of the Earth's core. *Academie des Sciences Paris Comptes Rendus Serie B Sciences Physiques*, *318*, 341–350.
- Riley, G. N., & Kohlstedt, D. L. (1991). Kinetics of melt migration in upper mantle-type rocks. *Earth Planet Science Letters*, *105*(4), 500–521.
- Romanowicz, B., & Gung, Y. (2002). Superplumes from the core-mantle boundary to the lithosphere: Implications for heat flux. *Science*, *296*(5567), 513–516.
- Sakairi, T., Ohtani, E., Kamada, S., Sakai, T., Sakamaki, T., & Hirao, N. (2017). Melting relations in the Fe–S–Si system at high pressure and temperature: implications for the planetary core. *Physics of the Earth and Planetary Interiors*, *4*(1), 10.
- Scott, T., & Kohlstedt, D. (2006). The effect of large melt fraction on the deformation behavior of peridotite. *Earth and Planetary Science Letters*, *246*(3), 177–187.
- Shimizu, H., Poirier, J. P., & Mouel, J. L. L. (2005). On crystallization at the inner core boundary. *Physics of the Earth and Planetary Interiors*, *151*(1), 37–51.
- Shirley, D. N. (1986). Compaction of igneous cumulates. *Journal of Geology*, *94*(6), 795–809.
- Smylie, D. (1999). Viscosity near Earth's solid inner core. *Science*, *284*(5413), 461–463.
- Smylie, D. E., Vadim, V. B., & Andrew, P. (2009). Direct observations of the viscosity of Earth's outer core and extrapolation of measurements of the viscosity of liquid iron. *Physics-Uspekhi*, *52*(1), 79.
- Solomatov, V. S., Olson, P., & Stevenson, D. J. (1993). Entrainment from a bed of particles by thermal convection. *Earth and Planetary Science Letters*, *120*(3-4), 387–393.
- Song, X., & Helmlinger, D. V. (1995). AP wave velocity model of Earth's core. *Journal of Geophysical Research*, *100*, 9817–9830.
- Souriau, A., & Poupinet, G. (1991). The velocity profile at the base of the liquid core from PKP (BC+ Cdiff) data: an argument in favour of radial inhomogeneity. *Geophysical Research Letters*, *18*(11), 2023–2026.
- Stewart, A. J., Schmidt, M. W., Westrenen, W., & Liebske, C. (2007). Mars: a new core-crystallization regime. *Science*, *316*, 1323–1325.
- Sumita, I., Yoshida, S., Kumazawa, M., & Hamano, Y. (1996). A model for sedimentary compaction of a viscous medium and its application to inner-core growth. *Geophysical Journal International*, *124*(2), 502–524.

- Terasaki, H., Kamada, S., Sakai, T., Ohtani, E., Hirao, N., & Ohishi, Y. (2011). Liquidus and solidus temperatures of a Fe–O–S alloy up to the pressures of the outer core: Implication for the thermal structure of the Earth's core. *Earth and Planetary Science Letters*, *304*(3), 559–564.
- Tian, D., & Wen, L. (2017). Seismological evidence for a localized mushy zone at the Earth's inner core boundary. *Nature Communications*, *8*(1), 165. <https://doi.org/10.1038/s41467-017-00229-9>
- Tkalcic, H. (2015). Complex inner core of the Earth: The last frontier of global seismology. *Reviews of Geophysics*, *53*, 59–94. <https://doi.org/10.1002/2014RG000469>
- Van der Hilst, R., De Hoop, M., Wang, P., Shim, S.-H., Ma, P., & Tenorio, L. (2007). Seismostratigraphy and thermal structure of Earth's core-mantle boundary region. *Science*, *315*(5820), 1813–1817. <https://doi.org/10.1126/science.1137867>
- van der Hilst, R. D., Widiyantoro, S., & Engdahl, E. R. (1997). Evidence for deep mantle circulation from global tomography. *Nature*, *386*(6625), 578–584.
- Wark, D. A., & Watson, E. B. (1998). Grain-scale permeabilities of texturally equilibrated, monomineralic rocks. *Earth and Planetary Science Letters*, *164*(3–4), 591–605.
- Waszek, L., & Deuss, A. (2011). Distinct layering in the hemispherical seismic velocity structure of Earth's upper inner core. *Journal of Geophysical Research*, *116*, B12313. <https://doi.org/10.1029/2011JB008650>
- Wong, J., Davies, C. J., & Jones, C. A. (2018). A Boussinesq slurry model of the F-layer at the base of Earth's outer core. *Geophysical Journal International*, *214*(3), 2236–2249.
- Yokoo, S., Hirose, K., Sinmyo, R., & Tagawa, S. (2019). Melting Experiments on Liquidus Phase Relations in the Fe-S-O Ternary System Under Core Pressures. *Geophysical Research Letters*, *46*, 5137–5145. <https://doi.org/10.1029/2019GL082277>
- Yu, W. C., & Wen, L. (2006). Seismic velocity and attenuation structures in the top 400 km of the Earth's inner core along equatorial paths. *Journal of Geophysical Research*, *111*, B07308. <https://doi.org/10.1029/2005JB003995>
- Zhang, Y., Sekine, T., He, H., Yu, Y., Liu, F., and Zhang, M. (2016). Experimental constraints on light elements in the Earth's outer core. *Scientific Reports*, *6*, 22473. <https://doi.org/10.1038/srep22473>
- Zhang, Y., Sekine, T., Lin, J.-F., He, H., Liu, F., Zhang, M., et al. (2018). Shock compression and melting of an Fe-Ni-Si alloy: implications for the temperature profile of the Earth's core and the heat flux across the core-mantle boundary. *Journal of Geophysical Research: Solid Earth*, *123*, 1314–1327. <https://doi.org/10.1002/2017JB014723>
- Zou, Z., Koper, K. D., & Cormier, V. F. (2008). The structure of the base of the outer core inferred from seismic waves diffracted around the inner core. *Journal of Geophysical Research*, *113*, B05314. <https://doi.org/10.1029/2007JB005316>